Slab melting as a barrier to deep carbon subduction

Andrew R. Thomson[1,2], Michael J. Walter[1], Simon C. Kohn[1] & Richard A. Brooker[1]

Interactions between crustal and mantle reservoirs dominate the surface inventory of volatile elements over geological time, moderating atmospheric composition and maintaining a life-supporting planet[1]. While volcanoes expel volatile components into surface reservoirs, subduction of oceanic crust is responsible for replenishment of mantle reservoirs[2,3]. Many natural, 'superdeep' diamonds originating in the deep upper mantle and transition zone host mineral inclusions, indicating an affinity to subducted oceanic crust[4–7]. Here we show that the majority of slab geotherms will intersect a deep depression along the melting curve of carbonated oceanic crust at depths of approximately 300 to 700 kilometres, creating a barrier to direct carbonate recycling into the deep mantle. Low-degree partial melts are alkaline carbonatites that are highly reactive with reduced ambient mantle, producing diamond. Many inclusions in superdeep diamonds are best explained by carbonate melt–peridotite reaction. A deep carbon barrier may dominate the recycling of carbon in the mantle and contribute to chemical and isotopic heterogeneity of the mantle reservoir.

Altered oceanic crust incorporates appreciable carbon, which is added by magmatic and hydrothermal processes[8], and by addition of CO_2 during interaction of basalt with sea water[9]. Together, these alteration processes result in subducting lithosphere that contains an average of ~2 weight per cent (wt%) CO_2 in the uppermost volcanic section and 100–5,000 p.p.m. CO_2 throughout the remaining 7 km of crust[8]. Crustal carbon initially contains a mixture of reduced hydrocarbons[8] and oxidized carbonates[9]. However, metamorphic re-equilibration of slab carbon with ferric iron and/or oxidizing fluids produced during serpentine dehydration at sub-arc conditions probably converts most slab carbon to carbonate[10]. Some of this carbon is returned to the exosphere in volcanic arcs, but both theoretical[11] and experimental[12] studies suggest that a considerable quantity of carbon may survive beyond slab dehydration, and be subducted into the mantle.

Carbon is insoluble in mantle silicate minerals[13] and is stored either as carbonate, carbide or diamond, depending on the oxidation state. Under oxidizing conditions, carbonate lowers the melting point (solidus) of mantle peridotite by up to 500 °C compared with volatile-free mantle[14]. However, at the more reducing conditions prevailing deeper in the upper mantle and transition zone, carbon will be stored as diamond or carbide minerals[15], where it does not appreciably influence melting.

Superdeep diamonds originate from depths beneath the lithospheric mantle ($\gtrsim$200 km) and are the only direct samples of the deep mantle carbon reservoir. Inclusions in these diamonds are dominated by upper mantle and transition zone minerals, which are mostly associated with subducted mafic lithologies rather than peridotite[4–7,16]. Many superdeep diamonds are made of isotopically light carbon[6,7] and, where measured, their inclusions contain isotopically heavy oxygen[17], unambiguously indicating an origin from recycled surface material[6,7,17]. The elevated trace element abundances of many silicate inclusions suggest crystallization from a low-degree melt, thought to be generated from melting of subducted oceanic crust[7,18]. Here we examine the fate of subducting carbonated mid-ocean-ridge basalt (MORB) as it reaches the transition zone, and the potential for melt–mantle reactions to reproduce superdeep diamonds and their distinctive inclusion assemblages.

Previous experimental studies have investigated the melting behaviour of carbonated basalt at elevated pressures, but only one extends beyond 10 GPa (ref. 19). These studies show a remarkable diversity in melting behaviour, making extrapolation to higher pressures difficult. In addition, the bulk compositions employed in previous studies often contain considerably more CO_2 than mean oceanic crust, and fall outside the compositional field of natural MORB rocks (see Methods, Extended Data Fig. 1 and Extended Data Table 1). To understand better the melting behaviour of deeply subducted oceanic crust, we determined the melting phase relations of a synthetic MORB composition containing 2.5 wt% CO_2 between 3 and 21 GPa (Methods). Our starting composition replicates the major element composition of basaltic rocks from International Ocean Discovery Program (IODP) hole 1256D[20] and falls within the range of natural crust compositions[21] (Extended Data Fig. 1).

We observe subsolidus phase assemblages containing garnet, clinopyroxene, a SiO_2 polymorph, and Ti-rich oxide at all pressures (Extended Data Figs 2, 3 and Extended Data Table 2). The carbon component was either CO_2, dolomite, magnesite or magnesite plus Na-carbonate depending on the pressure, and the positions of solid carbonate phase boundaries are consistent with previous studies[22,23]. Near-solidus partial melts are CO_2-bearing silicate melts below 7 GPa, and silica-poor calcic carbonatites above 7 GPa. The alkali component of carbonatite melts increases with pressure (Extended Data Fig. 4), and all melts have high TiO_2/SiO_2 (see Methods and Extended Data Figs 2–5, Extended Data Table 2 and Supplementary Tables 1–4 for detailed results).

The melting temperature of carbonated oceanic crust is tightly bracketed from ~3 to 21 GPa (Fig. 1). Melting temperatures increase steadily with increasing pressure until about 13 GPa, when the solidus dramatically drops over a narrow pressure interval by ~200 °C. This drop in solidus temperature is caused by a change in clinopyroxene composition towards a more sodium-rich composition above 13 GPa due to dissolution of sodium-poor pyroxene components into coexisting garnet. Eventually, clinopyroxene becomes so sodium-rich that a coexisting Na-carbonate mineral ($[Na_{0.97}K_{0.03}]_{0.33}[Ca_{0.86}Mg_{0.11}Fe_{0.03}]_{0.67}CO_3$) stabilizes in the subsolidus assemblage, causing the depression along the solidus. The loss of the sodium-poor clinopyroxene component, and the extended stability of sodic clinopyroxene in the absence of an alternative sodium-bearing silicate phase, is consistent with previous studies[24]. Above 16 GPa the solidus changes little with pressure, remaining at ~1,150 °C, consistent with the solidus observed in a sodium-rich simplified system in which sodic carbonate ($[Na,K]_{0.33}Ca_{0.67}CO_3$) controls melting temperatures[25]. The major difference between this work and the previous study of carbonated MORB above 8 GPa (ref. 19) is the different phase assemblage resulting from the lower and more realistic CO_2 and CaO contents of our bulk composition. Previous bulk compositions with higher CaO contents (Extended Data Figs 1 and 5) are located on the calcium-rich side of the majorite–clinopyroxene tie-line and stabilize aragonite as the carbon-hosting phase, which can incorporate
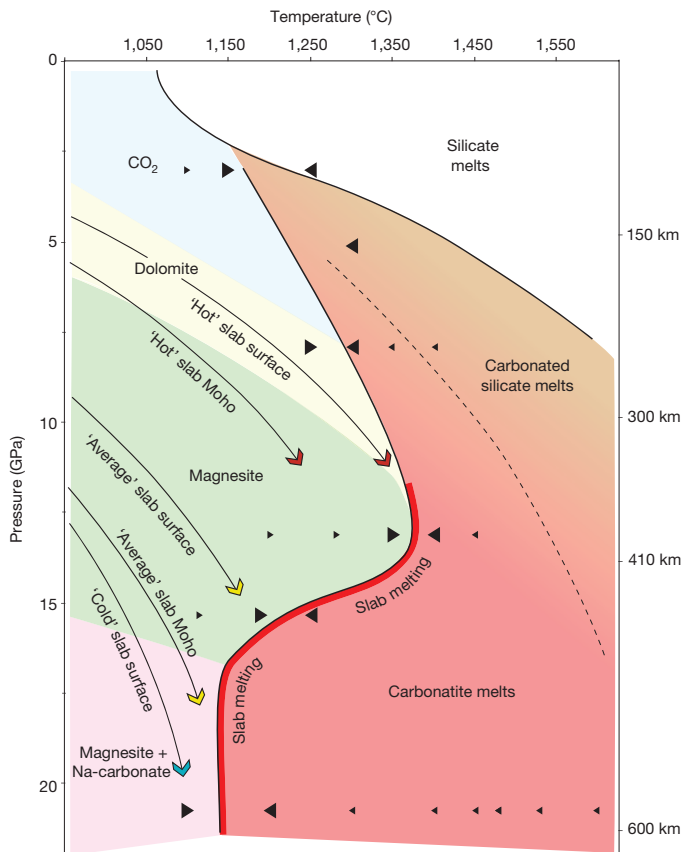
Figure 1 | The melting curve of carbonated MORB compared to hot and cold subduction geotherms[26]. The stability fields of carbon-bearing phases are identified in different colours. Experiments performed are marked by filled triangles indicating their relationship to the solidus, larger symbols mark solidus brackets. The solidus ledge creates a narrow depth interval where slab temperatures intersect the melting curve, producing a focused region of melt generation at the top of the transition zone.

considerable Na_2O. The lower CO_2 content in our bulk composition results in a smaller proportion of carbonate, of which the dominant species is sodium-poor magnesite. Thus, sodic clinopyroxene remains stable as an alkali-host, coexisting with stoichiometric Na-carbonate to high pressures.

The deep solidus depression in carbonated oceanic crust at uppermost transition zone conditions creates a key control on the recycling of mantle carbon. Extrapolation of the range of modern-day oceanic crustal geotherms into the transition zone[26] reveals that the majority of slabs will intersect our solidus for carbonated recycled MORB (Fig. 1), producing carbonatite melt. Given the expected temperature profile in the average subducted slab[26] we estimate that melting would occur to depths of at least 7 km into the crustal section. Only the coldest modern-day slabs escape the solidus depression and are able to carry their carbonate cargo beyond the transition zone. If ancient slabs were hotter[3], it seems likely that carbonate subduction through the transition zone and into the lower mantle has been limited throughout Earth's history. While the natural variability of subducting slabs (for example, composition, age, temperature) will have created some range in melting behaviour, the depression of the carbonated eclogite solidus will remain an efficient barrier. Thus, direct recycling of carbon into the lower mantle may have been highly restricted throughout most of the Earth's history, instead being redistributed throughout the upper mantle.

Carbonatitic melts are predicted to be mobile at mantle conditions due to their low viscosity and ability to wet silicate minerals[27], so should percolate out of the slab and infiltrate the overlying peridotitic mantle[25]. Experiments suggest that below ~250 km, ambient

mantle oxygen fugacity is reducing, and a free metal phase may be present in the mantle[28]. Under such conditions carbonate melt is unstable and will reduce to diamond plus oxygen by a 'redox-freezing' reaction[28] such as: $MgCO_3 + 2Fe^0 = 3(Mg_{0.33}, Fe^{2+}_{0.67})O + C$. Thus, the expulsion of carbonatite melts due to melting of oceanic crust along the solidus depression provides an ideal environment for diamond growth across a depth interval of ~300–700 km. We predict that the interaction between MORB-derived carbonatite melt and ambient peridotite is capable of reproducing many of the characteristics of superdeep diamonds and the mineral inclusions that they capture from this depth interval[4,5]. The most common silicate minerals identified in superdeep diamonds are majorite garnet, and a titanium-bearing, calcium-silicate phase commonly interpreted as retrogressed 'calcium perovskite'[4,6,7,18]. Barometric estimates of the crystallization pressures for these majorite inclusions indicate they crystallized between 10 and
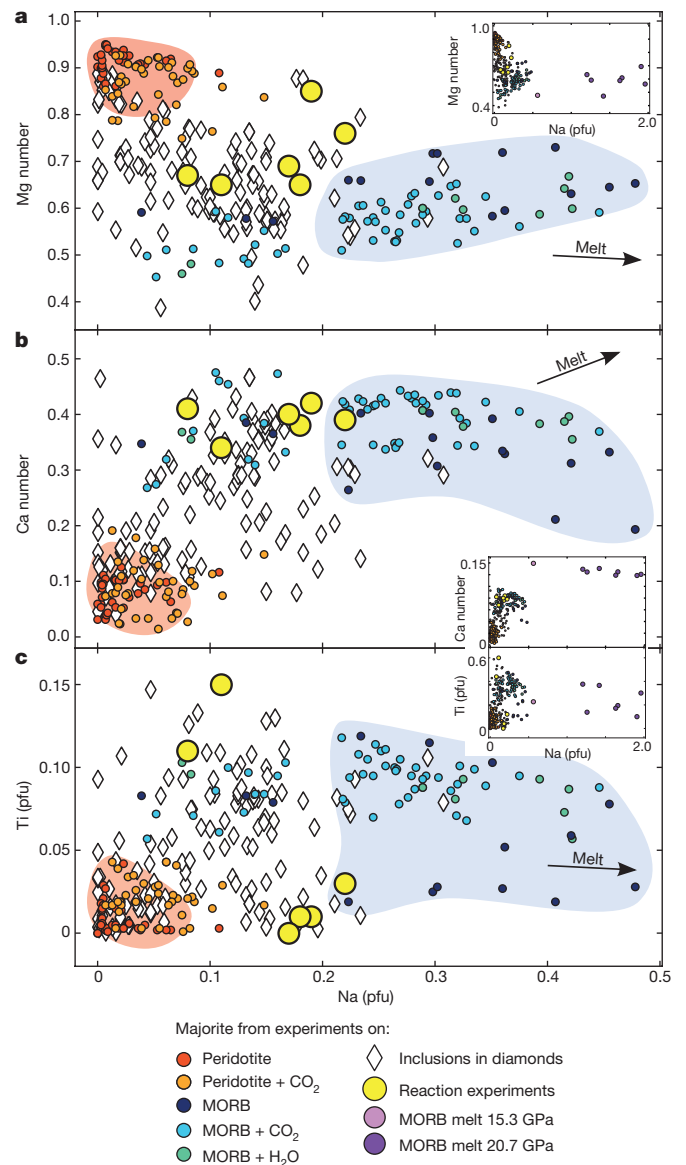

Figure 2 | Composition of majoritic garnet minerals from previous experimental studies, inclusions in diamonds and reaction experiments. a–c, The red field outlines the approximate range of peridotitic majorite compositions, the blue field outlines the range of MORB majorites from pressures above the carbonated MORB solidus ledge (≳9 GPa). Na (per formula unit (pfu)) plotted against Mg number (Mg number = Mg/[Mg+Fe]) (**a**), Ca number (Ca number = Ca/[Ca+Mg+Fe]) (**b**), and Ti (pfu) (**c**). Data and corresponding references for this figure are provided in the online source data file.

16 GPa (ref. 5), and inclusions of calcium perovskite are constrained by their chemistry to have formed between ~10 and 20 GPa (refs 6, 18). These pressures are remarkably consistent with the range of pressures at which slab crustal geotherms are predicted to intersect the carbonated solidus depression (Fig. 1).

Redox reactions in the mantle are complex and involve silicates, many containing iron that exists in both ferrous (Fe^{2+}) and ferric form (Fe^{3+}). To test the melt–mantle interaction model, we recreated the infiltration process in a second set of experiments by partially equilibrating a model slab melt with an iron-metal-bearing transition zone peridotite assemblage at 20 GPa (see Methods for details). We observe a reaction zone between the alkaline carbonatite melt and the initial peridotitic assemblage of majorite, wadsleyite, calcium-silicate perovskite and iron metal that consists of sodium-rich majoritic garnet, $Ca[Si,Ti]O_3$ perovskite, ferrous ringwoodite (Mg number ~75), ferropericlase (Mg number ~0.4) and diamond (Extended Data Figs 6, 7 and Extended Data Table 3). We compare the resulting mineral compositions with previous experimental data for peridotite and MORB systems to investigate whether natural inclusion assemblages might preserve a record of mineral-melt reactions.

The compositions of the majority of superdeep majoritic garnet inclusions are not typical of those expected in either peridotitic or eclogitic bulk compositions (Fig. 2) and instead lie between these two end-members. These intermediate compositions have previously been described as pyroxenitic, and it was suggested that the transition zone may harbour a large component of this rock type[16]. Our results suggest an alternative explanation. In Fig. 2 the majoritic garnets produced during the experimental melt–mantle interaction are intermediate between peridotitic and eclogitic compositions, and cover much of the range seen in the diamond inclusions. The chemical imprint imparted by the MORB carbonatite on the peridotitic mantle is recorded in the inclusions as elevated Ca number, Na and Ti contents alongside depleted Mg number. Our experiments only demonstrate the composition of garnets produced near the beginning of the melt–mantle interaction sequence, and we suggest that the intermediate character of the natural inclusions records a snapshot
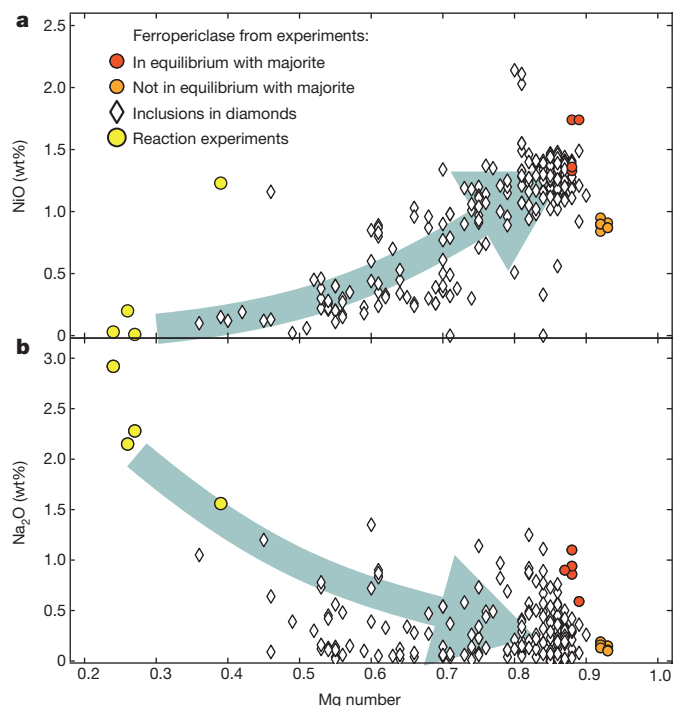

Figure 3 | Composition of ferropericlase minerals from previous experimental studies, inclusions in diamonds and reaction experiments. a, b, Blue arrows indicate the compositional evolution expected as melt–mantle interactions progress. Data and corresponding references for this figure are provided in the online source data file.

of the infiltration and reaction of slab-derived carbonatite melt with peridotite.

Experimental calcium perovskites have high titanium (~40–60 mol% $CaTiO_3$) and are essentially magnesium-free, features observed throughout the global range of 'calcium perovskite' inclusions
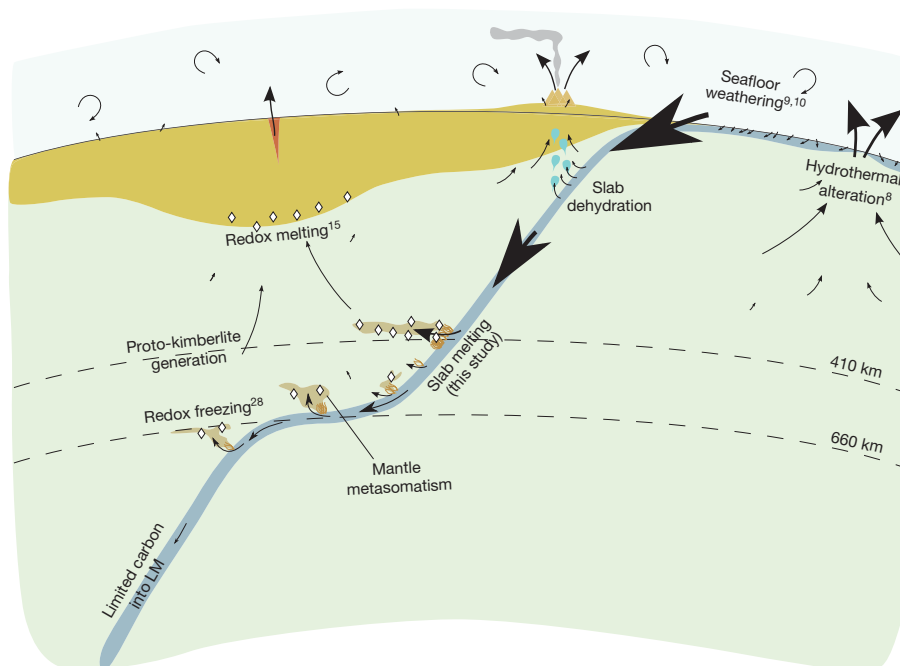
Figure 4 | Schematic of the deep mantle carbon cycle. Arrows represent paths and estimates of the relative magnitudes of carbon fluxes. Downwelling slabs dehydrate at sub-arc depths but retain the majority of their carbon cargo. Upon reaching the transition zone they produce carbonatite melts (this study) along the solidus ledge that infiltrate[28] and react with the overlying mantle (this study). This causes diamond production, refertilization and associated metasomatism of the surrounding mantle. The melting of recycled crust in the transition zone essentially prevents carbon transport into the lower mantle (LM).

(Extended Data Fig. 8). Thus, our reaction experiments reproduce the unique characteristics of diamond-hosted 'calcium perovskite' inclusions. Crystallization by reaction between a low-degree carbonated melt and peridotite is also consistent with the extremely elevated trace element contents of diamond-hosted 'calcium perovskites' inclusions[24].

Probably the most abundant inclusions in superdeep diamonds are magnesium-iron oxide ([Mg,Fe]O), which are often interpreted to indicate diamond growth in the lower mantle[4]. However, our experiments demonstrate that ferropericlase can be produced in reactions between carbonatitic melt and reduced mantle peridotite at upper mantle pressures rather than requiring a lower mantle origin[29]. Figure 3 demonstrates that natural ferropericlase inclusions are almost all iron-rich relative to ferropericlase expected in mantle peridotite, and their compositions form arrays towards higher NiO and lower Na_2O with increasing magnesium number. Our experimental ferropericlase compositions lie at the end of the arrays and are iron-rich because the peridotite starting material was initially iron-saturated. We suggest that, like the majorite inclusions, the array of intermediate ferropericlase compositions record the progressive reaction of carbonatite melt and ambient mantle.

The melting-phase relations of recycled oceanic crust suggest that slabs should undergo melting and loss of carbonate components in the transition zone (Fig. 4), a process that has considerable implications for the deep carbon cycle. The compositions of diamond-hosted inclusions provide strong evidence of this process and confirm that carbon must survive subduction beyond sub-arc dehydration reactions. We predict that carbon is rarely transported beyond the transition zone and instead refertilizes the upper mantle as diamond. Oxidation of diamond-bearing mantle upon upwelling can lead to redox melting[15] beneath the lithosphere and contribute markedly to the generation and geochemical signature of surface lavas. This process also probably contributes to the formation of distinctive chemical and isotopic reservoirs in the mantle[30]. Superdeep diamonds provide a physical record of carbon recycling above subducting slabs, which can be used to infer the residence time of carbon in the mantle. This residence time is regulated by rates of subduction, convective mantle upwelling and melting beneath the lithosphere, and could occur over a range of timescales, perhaps as short as tens to hundreds of millions of years, suggesting the mantle carbon cycle can be considerably more vigorous than previously estimated[2,3].

Online Content Methods, along with any additional Extended Data display items and Source Data, are available in the online version of the paper; references unique to these sections appear only in the online paper.

1. Zahnle, K. et al. Emergence of a habitable planet. Space Sci. Rev. **129,** 35–78 (2007).
2. Sleep, N. H. & Zhanle, K. Carbon dioxide cycling and implications for climate on ancient Earth. J. Geophys. Res. **106,** 1373–1399 (2001).
3. Dasgupta, R. & Hirschmann, M. M. The deep carbon cycle and melting in Earth's interior. Earth Planet. Sci. Lett. **298,** 1–13 (2010).
4. Harte, B. Diamond formation in the deep mantle: the record of mineral inclusions and their distribution in relation to mantle dehydration zones. Mineral. Mag. **74,** 189–215 (2010).
5. Stachel, T. Diamonds from the asthenosphere and the transition zone. Eur. J. Mineral. **13,** 883–892 (2001).
6. Thomson, A. R. et al. Origin of sub-lithospheric diamonds from the Juina-5 kimberlite (Brazil): constraints from carbon isotopes and inclusion compositions. Contrib. Mineral. Petrol. **168,** 1081 (2014).
7. Bulanova, G. et al. Mineral inclusions in sublithospheric diamonds from Collier 4 kimberlite pipe, Juina, Brazil: subducted protoliths, carbonated melts and primary kimberlite magmatism. Contrib. Mineral. Petrol. **160,** 489–510 (2010).
8. Shilobreeva, S., Martinez, I., Busigny, V., Agrinier, P. & Laverne, C. Insights into C and H storage in the altered oceanic crust: results from ODP/IODP Hole 1256D. Geochim. Cosmochim. Acta **75,** 2237–2255 (2011).
9. Alt, J. & Teagle, D. The uptake of carbon during alteration of ocean crust. Geochim. Cosmochim. Acta **63,** 1527–1535 (1999).
10. Debret, B. et al. Redox state of iron during high-pressure serpentinite dehydration. Contrib. Mineral. Petrol. **169,** 36 (2015).
11. Kerrick, D. M. & Connolly, J. A. D. Metamorphic devolatilization of subducted mid-ocean ridge metabasalts: implications for seismicity, arc magmatism and volatile recycling. Earth Planet. Sci. Lett. **189,** 19–29 (2001).
12. Poli, S., Franzolin, E., Fumagalli, P. & Crottini, A. The transport of carbon and hydrogen in subducted oceanic crust: an experimental study to 5 GPa. Earth Planet. Sci. Lett. **278,** 350–360 (2009).
13. Shcheka, S. S., Wiedenbeck, M., Frost, D. J. & Keppler, H. Carbon solubility in mantle minerals. Earth Planet. Sci. Lett. **245,** 730–742 (2006).
14. Ghosh, S., Ohtani, E., Litasov, K. & Terasaki, H. Solidus of carbonated peridotite from 10 to 20 GPa and origin of magnesiocarbonatite melt in the Earth's deep mantle. Chem. Geol. **262,** 17–28 (2009).
15. Stagno, V., Ojwang, D. O., McCammon, C. A. & Frost, D. J. The oxidation state of the mantle and the extraction of carbon from Earth's interior. Nature **493,** 84–88 (2013).
16. Kiseeva, E. S. et al. Metapyroxenite in the mantle transition zone revealed from majorite inclusions in diamonds. Geology **41,** 883–886 (2013).
17. Ickert, R. B., Stachel, T., Stern, R. A. & Harris, J. W. Extreme ^{18}O-enrichment in majorite constrains a crustal origin of transition zone diamonds. Geochem. Persp. Lett. **1,** 65–74 (2015).
18. Walter, M. J. et al. Primary carbonatite melt from deeply subducted oceanic crust. Nature **454,** 622–625 (2008).
19. Kiseeva, E. S., Litasov, K. D., Yaxley, G. M., Ohtani, E. & Kamenetsky, V. S. Melting and phase relations of carbonated eclogite at 9–21 GPa and the petrogenesis of alkali-rich melts in the deep mantle. J. Petrol. **54,** 1555–1583 (2013).
20. Expedition 309/312 Scientists. Site 1256. In Superfast Spreading Rate Crust 2 and 3 (eds Teagle, D. A. H. et al.) Vol. 309/312 of Proc. IODP http://dx.doi.org/10.2204/iodp.proc.309312.103.2006 (Integrated Ocean Drilling Program Management International, Inc., 2006).
21. Gale, A., Dalton, C. A., Langmuir, C. H., Su, Y. & Schilling, J.-G. The mean composition of ocean ridge basalts. Geochem. Geophys. Geosyst. **14,** 489–518 (2013).
22. Martin, A. M., Laporte, D., Koga, K. T., Kawamoto, T. & Hammouda, T. Experimental study of the stability of a dolomite + coesite assemblage in contact with peridotite: implications for sediment-mantle interaction and diamond formation during subduction. J. Petrol. **53,** 391–417 (2012).
23. Luth, R. W. Experimental determination of the reaction aragonite + magnesite = dolomite at 5 to 9 GPa. Contrib. Mineral. Petrol. **141,** 222–232 (2001).
24. Okamoto, K. & Maruyama, S. The Eclogite–Garnetite transformation in the MORB + H_2O system. Phys. Earth Planet. Inter. **146,** 283–296 (2004).
25. Litasov, K., Shatskiy, A., Ohtani, E. & Yaxley, G. Solidus of alkaline carbonatite in the deep mantle. Geology **41,** 79–82 (2013).
26. Syracuse, E. M., van Keken, P. E. & Abers, G. A. The global range of subduction zone thermal models. Phys. Earth Planet. Inter. **183,** 73–90 (2010).
27. Hammouda, T. & Laporte, D. Ultrafast mantle impregnation by carbonatite melts. Geology **28,** 283–285 (2000).
28. Rohrbach, A. & Schmidt, M. W. Redox freezing and melting in the Earth's deep mantle resulting from carbon–iron redox coupling. Nature **472,** 209–212 (2011).
29. Brey, G. P., Bulatov, V., Girnis, A., Harris, J. W. & Stachel, T. Ferropericlase—a lower mantle phase in the upper mantle. Lithos **77,** 655–663 (2004).
30. Jackson, M. G. & Dasgupta, R. Compositions of HIMU, EM1 and EM2 from global trends between radiogenic isotopes and major elements in ocean island basalts. Earth Planet. Sci. Lett. **276,** 175–186 (2008).

Supplementary Information is available in the online version of the paper.

Author Contributions A.R.T. designed, performed and analysed the experiments, gathered data from the literature and wrote the manuscript as part of his PhD studies. M.J.W. and S.C.K. provided training in experimental techniques, assisted during interpretation of results, provided advice and assisted with manuscript preparation in their roles as A.R.T.'s PhD supervisors. R.A.B. provided training and assistance with experimental techniques and sample preparation alongside contributing to the scientific content and preparation of the manuscript.

Author Information Reprints and permissions information is available at www.nature.com/reprints. The authors declare no competing financial interests. Readers are welcome to comment on the online version of the paper. Correspondence and requests for materials should be addressed to A.R.T. (a.r.thomson@ucl.ac.uk).

METHODS

Starting materials. The starting material for experiments to determine the melting-phase relations of carbonated MORB (ATCM1) replicates basalts from the IODP 1256D from the Eastern Pacific Rise[20] (the reported composition of IODP 1256D basalts is the average of all analyses presented in table T17 of ref. 20) with an added 2.5 wt% CO_2 (Extended Data Table 1). This material was formed by mixing high-purity SiO_2, TiO_2, Al_2O_3, FeO, MnO, MgO, $Ca_3(PO_4)_2$ and $CaCO_3$, which were fired overnight at temperatures of 400–1,000 °C, of appropriate weights in an agate mortar under ethanol. This mixture was decarbonated and fused into a crystal-free glass in a one-atmosphere tube furnace by incrementally increasing the temperature from 400 to 1,500 °C before drop quenching into water. Subsequently weighed amounts of $CaCO_3$, Na_2CO_3 and K_2CO_3 were ground into the glass, introducing the alkali and CO_2 components. After creation, the starting material was stored at 120 °C to avoid absorption of atmospheric water. Starting material ATCM2 replicates the near-solidus melt composition measured in melting experiments at 20.7 GPa and 1,400/1,480 °C. This was created by grinding natural magnesite and synthetic siderite with high-purity $CaCO_3$, Na_2CO_3, K_2CO_3, SiO_2, TiO_2, Al_2O_3 and $Ca_3(PO_4)_2$. Synthetic siderite was created in a cold-seal pressure vessel experiment run at 2 kbar and 375 °C for 7 days. A double Au capsule design containing iron (II) oxalate dehydrate in the inner and a 1:1 mixture of $CaCO_3$ and SiO_2 in the outer capsule produced a pale beige powder confirmed as siderite using Raman spectroscopy. The material for a sandwich experiment, to ensure near-solidus melt compositions were accurately determined at 20.7 GPa, was formed of a 3:1 mixture of ATCM1:ATCM2.

The transition-zone peridotite mineral assemblage in reaction experiments was synthesized at 20.7 GPa and 1,600 °C for 8 h from a mixture of KR4003 natural peridotite[31] with an added 2.5 wt% Fe metal. In reaction runs the recovered synthetic peridotite was loaded in a second capsule, surrounded by the ATCM2 near-solidus melt composition. Additional reaction-type experiments were performed on ground mixtures of peridotite and melt compositions. In these experiments PM1 pyrolite[32] was used as the peridotite component and mixed with ATCM2 melt in 9:1, 7:3 and 1:1 weight ratios in Fe capsules. A single mixed experiment was performed in a Au capsule and used a starting mix of PM1:Fe:ATCM2 in 16:1:4 molar ratio.

Experimental techniques. High-pressure experiments were performed using a combination of end-loaded piston cylinder (3 GPa) and Walker-type multi anvil (5–21 GPa) experiments at the University of Bristol. Piston cylinder experiments employed a NaCl-pyrex assembly with a straight graphite furnace and Al_2O_3 inner parts. Temperature was measured using type D thermocouple wires contained in an alumina sleeve and positioned immediately adjacent to the $Au_{80}Pd_{20}$ sample capsule that contained the powdered starting material. We assume that the temperature gradient across the entire capsule (<2 mm) was smaller than 20 °C (refs 33, 34). The hot piston-in technique was used with a friction correction of 3% applied to the theoretical oil pressure to achieve the desired run conditions[35].

Multi-anvil experiments were performed using Toshiba F-grade tungsten carbide cubes bearing 11, 8 or 4 mm truncated corners in combination with a pre-fabricated Cr-doped MgO octahedron of 18, 14 or 10 mm edge length, respectively. The relationship between oil-reservoir and sample pressure for each cell was calibrated at room and high temperature (1,200 °C) by detecting appropriate room temperature phase transitions of Bi, ZnTe and GaAs and bracketing transformations of SiO_2 (quartz-coesite and coesite-stishovite), Mg_2SiO_4 (α-β and β-γ) and $CaGeO_3$ (garnet-perovskite). Calibrations are estimated to be accurate within ±1 GPa. In all experiments, desired run pressure was achieved using a slow, Eurotherm controlled, pressure ramp of ≤50 tonnes per hour. Experiments were heated after high pressure was reached with high temperatures generated using stepped graphite (18/11 cell) or straight $LaCrO_3$ furnaces (14/8 and 10/4 cells) and monitored with type C thermocouple wires. Two 10/4 experiments, performed during a period of repeated $LaCrO_3$ heater failures, used rolled 40-μm-thick Re furnaces. Temperature was quenched by turning off the furnace power before a slow decompression ramp (half the rate of experiment compression) to ambient conditions. Samples were contained in Au capsules unless temperatures exceeded its thermal stability, in which case $Au_{80}Pd_{20}$ or $Au_{75}Pd_{25}$ capsules were used. Run durations all exceeded 600 min and are reported in Extended Data Tables 2 and 3. Temperature uncertainties were believed to be less than ±20, 30 or 50 °C for 18/11, 14/8 and 10/4 cells respectively[36,37].

Recovered samples were mounted longitudinally in epoxy, polished under oil and repeatedly re-impregnated with a low viscosity epoxy (Buelher EpoHeat) to preserve soft and water-soluble alkali carbonate components present in run products.

Analytical techniques. Polished and carbon-coated run products were imaged in backscatter electron mode (BSE) using a Hitachi S-3500N scanning electron microscope (SEM) with an EDAX Genesis energy dispersive spectrometer to identify stable phases and observe product textures. Subsequently, wavelength dispersive spectroscopy (WDS) was performed using the Cameca SX100 Electron Microprobe or the Field Emission Gun Jeol JXA8530F Hyperprobe at the University of Bristol to achieve high-precision chemical analyses of run products. Analyses were performed using an accelerating voltage of 15 or 12 kV on the respective instruments, with a beam current of 10 nA. Calibrations were performed during each session using a range of natural mineral and metal standards and were verified by analysing secondary standards (as described previously[6]). Silicate phases were measured using a focused electron beam whereas carbonates and melts were analysed using an incident beam defocused up to a maximum size of 10 μm. Count times for Na and K were limited to 10 s on peak and 5 s on positive and negative background positions. Peak count times for other elements were 20–40 s. Additional analyses of the calcium perovskite phases grown during reaction experiments, measuring only SiO_2 and MgO content, were made using the Jeol instrument at 5 kV and 10 nA to ensure reported MgO contents were not influenced by secondary fluorescence from surrounding material.

The identity of experimental-produced minerals was determined using Raman spectroscopy as a fingerprint technique. Spectra were collected using a Thermo Scientific DXRxi Raman microscope equipped with an excitation laser of either 455 or 532 nm.

Choice of bulk composition and comparison with previous studies. Studies that investigate the alteration of oceanic crust have demonstrated that carbon incorporation does not simply occur by the addition of a single carbonate species to MORB[9]. It instead appears to occur by a complex amalgamation of hydrocarbon and graphite deposition related to hydrothermal fluxing above magma chambers at the mid-ocean ridge[8] and underwater weathering[9,38–40] where seawater-derived CO_2 reacts with leached crustal cations, often in veins. It is believed that the quantity of biotic organic carbon in the crustal assemblage is negligible compared with abiotic organic compounds and inorganic carbonates[8]. These processes result in a layered crustal assemblage that, in the uppermost few hundred metres can contain up to a maximum of 4 wt% CO_2 in rare cases[9,39] but more commonly <2 wt% CO_2 (refs 8, 9, 39). Beneath 500 m depth the carbon content drops to between 100 and 5,000 p.p.m. CO_2 throughout the remainder of the 7-km-thick basaltic section[8], and is mostly organic hydrocarbon species. The upper 300 m are regularly altered and can be generally thought to have compositions similar to the altered MORB rocks analysed previously[41]. Deeper portions of the MORB crust retain their pristine MORB compositions. It is therefore apparent that carbonated eclogite bulk compositions used in previous studies, where at least 4.4 wt% CO_2 was added to an eclogite by addition of ~10 wt% carbonate minerals, may not be good analogues of naturally subducting crustal sections. The compositions of these starting materials from previous studies[19,42–46] can be found in Extended Data Table 1. We do not include the composition of the starting material used by refs 47 or 48 as these studies were conducted in simplified chemical systems so are not directly comparable with these natural system compositions.

However, as some of the previous studies rightly identify and discuss, the composition of deeply subducted MORB is unlikely to be the same as that entering the subduction system. One process widely believed to alter the composition of downwelling MORB is sub-arc slab dehydration. Pressure (P)–temperature (T) paths of subducted slabs[26] can be compared with experimental studies of hydrous, carbonated and H_2O-CO_2-bearing eclogite compositions[12,24,42,43,49] and thermodynamic models[11,50] to conclude that slabs experience dehydration at sub-arc conditions (that is, 1–5 GPa) but will generally not reach high enough temperatures to undergo melting. Therefore, they will by and large retain their carbon components although some fraction may be lost by dissolution into aqueous fluids[51,52]. It is believed that sub-arc dehydration is capable of removing SiO_2 from the subducting assemblage, and previous carbonated MORB compositions were therefore designed to be considerably silica undersaturated (relative to fresh/altered MORB)[19,43–45]. While studies[53–56] do indicate that SiO_2 can become soluble in H_2O at high pressures, they infer that the solubility of silica in hydrous fluids only exceeds ~1 wt% at $T > 900$ °C at 1 GPa (higher T at higher P). In contrast, slab dehydration occurs on all prograde slab paths at $T < 850$ °C. Additionally, the composition of quenched hydrous fluids coexisting with MORB at 4 GPa and 800 °C (ref. 57) indicate that a maximum of ~12 wt% SiO_2 can dissolve in the fluid. Given that there should be considerably less than 10 wt% H_2O (more likely $<< 5$ wt% H_2O) in subducting assemblages, this suggests a maximum SiO_2 loss in subducting MORB lithologies of ~0.6–1.2 wt%. The compositions used in previous studies have SiO_2 depletions ranging from 3 wt% up to, more commonly, 6–10 wt% SiO_2 relative to MORB.

We further investigated the effect of oceanic crust alteration and sub-arc dehydration on the composition of subducted MORB rocks by compiling a data set of altered MORB[41] and exhumed blueschist, greenschist and eclogite facies rocks from exhumed terrains worldwide to compare them with fresh MORB[21], our starting

material and previous starting materials. We then assess the relevance of our starting material based on the composition of natural MORB rocks, rather than using models of the subduction process that contain few observable constraints. Results of this comparison are plotted in Extended Data Fig. 1. This analysis confirms that relative to fresh MORB, altered MORB and exhumed crustal rocks are somewhat depleted in SiO_2, up to a maximum of 6 wt% SiO_2 in the most extreme case, but more commonly 0–3 wt% SiO_2. Thus, many previous starting materials are too silica undersaturated to be good analogues of subducting MORB. Furthermore, this analysis reveals that altered and exhumed MORB are not enriched in CaO compared with fresh MORB, if anything they actually contain lower CaO on average. In contrast, all previous starting materials are enriched in CaO compared with fresh MORB. This is because most previous studies introduced the carbon component to their experiment by adding ~10 wt% calcite to an eclogite-base composition. We note that SLEC1 (ref. 43) was not created in this manner, but instead this composition falls far from the MORB field as the authors used an eclogite xenolith erupted by a Hawaiian volcano as a base material. By plotting the position of the maj–cpx join, defined by the composition of our experimental phases plotted in Extended Data Fig. 5, onto Extended Data Fig. 1a, we demonstrate that our bulk composition (ATCM1), ALL-MORB[21], the vast majority of the fresh MORB field, altered[41] and exhumed MORB samples fall on the CaO-poor side of this join, that is, on the Mg+Fe-rich side. Therefore, magnesite will be the stable carbonate phase in these compositions at high pressure (above dolomite breakdown). In contrast, all previous bulk compositions plot on the Ca-rich side of this join, or are very depleted in SiO_2, and therefore fall in a different phase field to the overwhelming majority of subducted MORB. This difference causes a considerable difference in the phase relations of our starting material relative to those used in previous studies.

We acknowledge that no single bulk composition can be a perfect analogue for the entire range of subducting MORB compositions, however, ATCM1 is a good proxy for sections of the MORB crust between ~300 m and 7 km depth that have unaltered major element compositions and low CO_2 contents. Additionally, ATCM1 remains a better analogue for the uppermost portions of the MORB crust than starting materials employed in previous studies because its CO_2 content is within the range of natural rocks while it is also not oversaturated in CaO or over depleted in SiO_2. This is despite it falling towards the SiO_2-rich end of the compositional spectrum of subducting MORB rocks.

Slab fO_2 and carbonate survival to transition zone conditions. Recent experiments have suggested that carbonate in eclogitic assemblages may be reduced to elemental carbon, either graphite or diamond, at depths shallower than 250 km (ref. 58). However, subducting slab geotherms are much colder than the experimental conditions investigated by this study, and additionally they are believed to contain considerable ferric iron that is further increased during de-serpentinization[10]. Indeed, several observations of carbonate inclusions in sub-lithospheric diamonds[6,7,59] require that slab carbon remains oxidized and mobile until diamond formation, far deeper than 250 km. Given the numerous observations from natural diamond samples, the general uncertainty in the mantle's fO_2 structure and the lack of any conclusive experimental evidence that subducting carbon becomes reduced before reaching the transition zone we posit that nearly all subducting carbon is stable as carbonate throughout the upper mantle in subducting MORB assemblages.

Carbonated MORB melting. Extended Data Table 2 presents the run conditions, durations and phase proportions in all carbonated MORB melting experiments, which are also summarized in Extended Data Fig. 2. Phase and melt compositions are presented in the Supplementary Tables 1–4. Phase proportions are calculated by mass balance calculations that use the mean composition of each phase as well as the reported 1σ uncertainty in this mean as inputs. We note that the 1σ uncertainty for some oxides in garnet and clinopyroxene minerals occasionally exceeds 1 wt%, although it is normally much smaller than this. These large uncertainties are a function of the small crystal sizes present in some runs, and not a function of sluggish reaction kinetics. Phase proportion calculations were run in a Monte Carlo loop of 10,000 calculation cycles where a varying random error was added to each oxide in each mineral phase during each iteration. Overall the distribution of varying random errors for each oxide form a Gaussian distribution with standard deviation equal to the reported 1σ uncertainty of measurements. The reported proportions are the numerical mean of all calculation cycles and the r^2 value reports the average squared sum of residuals. Low r^2 values indicate that chemical equilibrium is likely to have been achieved and that mineral and melt compositions have been accurately determined.

Representative BSE images of the polished experiments are shown in Extended Data Fig. 3. Garnets in experiments at all pressures contain abundant SiO_2 inclusions. In subsolidus experiments the number of inclusions increases and the definition of mineral boundaries deteriorates, which makes accurate analysis of garnet

compositions increasingly challenging. In supersolidus runs, garnet minerals adjacent, or near to, carbonatite melt pools have well defined edges and contain fewer inclusions. However, far from quenched melts the textures of garnets remain small and pervasively filled with inclusions, indicating the influence of melt fluxing on mineral growth. With increasing pressure, garnets become increasingly majoritic, with increasing quantities of octahedral silicon.

Clinopyroxene was observed in all subsolidus experiments, as euhedral crystals that are often spatially associated with the carbon-bearing phase. Cpx abundance falls with increasing pressure and their compositions becoming increasingly dominated by sodic components (jadeite, aegerine and $NaMg_{0.5}Si_{2.5}O_6$) at high pressure (Extended Data Fig. 5). Cpx only disappears from the stable phase assemblage in supersolidus experiments at 20.7 GPa. SiO_2 is observed in all runs and are small, often elongated tabular-shaped crystals. An oxide, either TiO_2 at low pressure or an Fe-Ti oxide above 13 GPa (as described previously[24]) are observed in all subsolidus runs.

The carbon-bearing phase in subsolidus experiments changes with increasing pressure. At 3 GPa CO_2, marked by the presence of voids in the polished sample, is stable. This converts to dolomite at 7.9 GPa, consistent with the position of the reaction $2cs + dol = cpx + CO_2$ (ref. 22). Beyond ~9 GPa dolomite becomes unstable and breaks down into magnesite + aragonite[23]. Therefore, because the ATCM1 bulk composition lies on the Mg+Fe^{2+}-rich side of the garnet–cpx join (Extended Data Figs 1a and 5), magnesite replaces dolomite as the carbon host in the experimental phase assemblage. This differs from experiments in previous studies, where aragonite was dominant because bulk compositions fall on the opposite side of the garnet–cpx join. It is clear from the ternary diagrams (Extended Data Fig. 5) that while the tie-line between garnet and cpx remains, magnesite and aragonite cannot coexist in a MORB bulk composition. Finally, at pressures above 15 GPa, Na-carbonate becomes stable in the subsolidus phase assemblage. This is chemographically explained by the rotation of the garnet–cpx tie-line with increasing pressure (EDF5). Its appearance can also be justified as a necessary host of sodium at increasing pressure, since aside from clinopyroxene there is no other Na-rich phase stable on the Mg+Fe side of the maj–cpx join.

The appearance of silicate melt, containing dissolved CO_2 (estimated by difference), defines the solidus at 3 GPa. This may initially appear to contradict the results of some previous studies, which find carbonatite melts are produced near the solidus of carbonated eclogite at pressures lower than 7 GPa (refs 43, 45, 46). However, this is easily explained by the differences in CO_2 and SiO_2 content used in these studies. The higher CO_2 and lower SiO_2 contents of previous studies stabilize carbonate melt to lower temperatures relative to silicate melts. Indeed, we note that our results are consistent with those described previously[42,44] (the two previous studies with the least depleted SiO_2), which also observed that near-solidus melts below 5 GPa were basaltic to dacitic silicate melts containing dissolved CO_2. The results of one paper[19] are not entirely self-consistent, in that at some pressures between 3.5 and 5.5 GPa the authors observed silicate melts before carbonate melts (4.5 and 5 GPa), whereas this relationship is sometimes reversed (5 GPa in AuPd capsules) or both melts were observed together (3.5 GPa). The observation of two immiscible melts in previous studies probably reflects the maximum CO_2 solubility in silicate melts. Since our bulk composition has less CO_2, akin to natural rocks, we do not observe liquid immiscibility.

In all experiments above 7 GPa, near-solidus melt compositions are carbonatititc and essentially silica-free. This result is notably different from those described previously[19], which reported that near-solidus melts were a mixture of silicate, carbonated silicate and carbonatite melts. We believe this contrast is caused by the interpretation of experimental run textures. Whereas ref. 19 identified regions of fine-grained material consisting of mixtures of stable phases from elsewhere in the capsule as quenched melts, we have not followed the same interpretation of these features. Although we do recognize similar features in some run products, we have interpreted these features as a consequence of poor crystal growth in regions far from the influence of melt fluxing. In all supersolidus experiments, we observed regions of carbonatite material (typically <1 wt% SiO_2) that is fully segregated from surrounding silicate minerals and possesses a typical carbonate-melt quench texture (Extended Data Fig. 3). Silicate minerals in close proximity to these melt pools are larger than those elsewhere in the same experiment, have well-defined crystal boundaries and contain few inclusions. Therefore, we attribute the variable texture and regions of fine-grained material present in experiments to the location of melt within experiments, which has a tendency to segregate to isolated regions of capsules under influence of temperature gradients. Although melt segregation occurs in all supersolidus experiments, the efficiency of segregation and size of melt pools considerably increases with rising temperature above the solidus. Extended Data Figure 4 shows the highly systematic evolution of the melt compositions reported from our study with increasing pressure, strongly supporting our interpretations.

Carbonatite melts are calcic, Ca number > 0.5 (Ca number = Ca/[Ca+Mg+Fe]), despite subsolidus carbonates being dominated by magnesite (Extended Data Fig. 4). Melts have high concentrations of TiO_2 (typically 1–3.5 wt%), P_2O_5 (0.4–1.5 wt%) and K_2O (0.3–1.5 wt%) and a variable Mg number (0.33–0.7 defined as Mg/[Mg+Fe]). The alkali content of melts, strongly dominated by Na_2O due to the bulk composition, increases with pressure (from 1 to ~15 wt% Na_2O at 7.9 and 20.7 GPa respectively; Extended Data Fig. 4). This increasing Na_2O content is driven by the decreasing compatibility of Na_2O in the residual mantle phase assemblages as the abundance of stable clinopyroxene falls. At 20.7 GPa the melt composition, as evidenced both by constant phase proportions and consistent melt/majorite compositions, remains constant over a temperature interval of ~350 °C above the solidus. It is only when temperature reaches 1,530–1,600 °C (runs #16 and #31) that the silica content of the melt begins to increase (to 8.7 wt%) and CO_2 content falls as melts start to become silica-carbonatites.

One experiment (#33) aimed to verify that measured low-degree melt compositions are accurate, and are not affected by analytical problems related to the small size of melt pools, was conducted at 20.7 GPa. In this experiment the abundance of carbonate melt was increased by adding a mix replicating the low degree melt composition ATCM2 to ATCM1 in a mass ratio of 1:3. If the composition of low-degree melts has been accurately determined in 'normal' experiments then this addition will have a negligible effect on phase relations or the compositions of the garnet, SiO_2 or melt; it would simply increase the melt abundance. The result of this experiment has a similar texture to all other experiments, where carbonatite melt segregates to one end of the capsule and is adjacent to large, well-formed majoritic garnets. The far end of the capsule has a much smaller crystal size, crystals have ragged edges, garnets are full of inclusions and SiO_2 is present along grain-boundaries and triple junctions (Extended Data Fig. 3h). Mineral and melt compositions, although not exactly identical, are similar to those measured in 'normal' experiments (to achieve identical compositions an iterative approach would be required that was not deemed to be necessary) thus confirming that near-solidus melt compositions have been accurately determined. The presence of fine-grained material away from segregated melt also acts to further confirm our hypothesis regarding the vital importance of melt presence for growing large crystals during experiments.

Subsolidus carbonate species at high pressure. Comparing our starting material and results with those of previous studies using ternary and quaternary projections (Extended Data Fig. 5) reveals that it is not possible for both magnesite and aragonite to coexist alongside majorite and clinopyroxene owing to stable mineral phase fields (see earlier). Thus, in Mg-Fe-dominated compositions, such as our starting material, magnesite is the stable carbonate at high-pressure subsolidus conditions. Whereas in Ca-dominated compositions aragonite will be the stable carbonate beyond the pressure of dolomite dissociation. Natural subducting MORB compositions, which contain, at most, a similar quantity of CO_2 to our bulk composition[11], almost all lie on the Ca-poor side of the majorite–clinopyroxene join (Extended Data Figs 1 and 5). In this situation, as our experiments demonstrate, cpx remains an important Na-host in MORB assemblages to high pressures alongside $[Na,K]_{0.33}Ca_{0.67}CO_3$ structured carbonate. Ca-rich compositions containing subsolidus $CaCO_3$ experience different phase relations because aragonite can dissolve considerable Na_2O and so is the sole Na-host in these compositions. We conclude that because the majority of natural MORB rocks fall on the Mg+Fe side of the maj–cpx join, like our bulk composition, that the phase relations determined in this study are applicable to the case of natural subduction. Therefore, the melting point depression we observe along the carbonated MORB solidus at uppermost transition zone pressures is generally applicable to subducted oceanic crust.

Melt–mantle reactions. Without the influence of slab-derived melts, the anhydrous transition zone peridotite assemblage at 20.7 GPa and 1,600 °C (experiment G168 and G176) is dominated by Na-poor majorite and wadsleyite (Mg number = 0.90) (Extended Data Fig. 6, Extended Data Table 3 and Supplementary Table 5a). Upon reaction with the near-solidus alkaline carbonatite defined during melting experiments, ATCM2, a clearly defined reaction zone is observed between this ambient peridotite assemblage and the infiltrating melt (Extended Data Fig. 6). The products of this reaction are garnet containing a notable $Na_2X^{2+}Si_5O_{12}$ majorite component, $Ca(Si,Ti)O_3$ perovskite, ringwoodite, ferropericlase and diamond. All of these phases were identified using Raman spectroscopy (Extended Data Fig. 7) and their compositions are presented in Supplementary Table 5a. Raman spectroscopy alone, which was performed before any sample polishing using diamond-based products, confirms the creation of diamond during these reactions. We have not observed diamond using SEM techniques and believe that it resides as sub-micrometre-sized inclusions in the various reaction-product minerals where it is seen by spectroscopic methods. The experiments performed on intimately mixed powders of melt and pyrolite also form the same phase assemblages (Extended Data Table 3) and mineral compositions from those runs are also presented in Supplementary Table 5b, c.

We observed the reaction products as new crystals floating in the residual carbonatite melt and/or nucleated on the relics of the peridotite assemblage, thus creating zoned minerals. We have demonstrated that the composition of majoritic minerals crystallizing during the reactions lie between those expected for peridotitic and eclogitic minerals at a similar pressure and possibly explain intermediate-composition diamond-hosted majorites (Fig. 2). We suggest that the full range of intermediate inclusion compositions might be created by the gradual shift in phase compositions, from those we observe towards more peridotitic minerals as the melt composition reacts with increasing quantities of mantle material. Additionally we have shown that the compositions of calcium perovskite (Extended Data Fig. 8) and ferropericlase (Fig. 3) formed during the reactions are consistent with diamond-hosted minerals of those species. Further experiments, across the solidus ledge and into the uppermost lower mantle pressure range are required to test whether melt–mantle interactions account for all diamond-hosted inclusions.

31. Walter, M. J. Melting of garnet peridotite and the origin of komatiite and depleted lithosphere. *J. Petrol.* **39,** 29–60 (1998).
32. Walter, M. J., Nakamura, E., Trönnes, R. G. & Frost, D. J. Experimental constraints on crystallization differentiation in a deep magma ocean. *Geochim. Cosmochim. Acta* **68,** 4267–4284 (2004).
33. Watson, E., Wark, D., Price, J. & Van Orman, J. Mapping the thermal structure of solid-media pressure assemblies. *Contrib. Mineral. Petrol.* **142,** 640–652 (2002).
34. Schilling, F. & Wunder, B. Temperature distribution in piston-cylinder assemblies: numerical simulations and laboratory experiments. *Eur. J. Mineral.* **16,** 7–14 (2004).
35. McDade, P. *et al.* Pressure corrections for a selection of piston-cylinder cell assemblies. *Mineral. Mag.* **66,** 1021–1028 (2002).
36. Walter, M. J., Thibault, Y., Wei, K. & Luth, R. W. Characterizing experimental pressure and temperature conditions in multi-anvil apparatus. *Can. J. Phys.* **73,** 273–286 (1995).
37. Hernlund, J., Leinenweber, K., Locke, D. & Tyburczy, J. A. A numerical model for steady-state temperature distributions in solid-medium high-pressure cell assemblies. *Am. Mineral.* **91,** 295–305 (2006).
38. Nakamura, K. & Kato, Y. Carbonatization of oceanic crust by the seafloor hydrothermal activity and its significance as a CO_2 sink in the Early Archean. *Geochim. Cosmochim. Acta* **68,** 4595–4618 (2004).
39. Coogan, L. a. & Gillis, K. M. Evidence that low-temperature oceanic hydrothermal systems play an important role in the silicate-carbonate weathering cycle and long-term climate regulation. *Geochem. Geophys. Geosyst.* **14,** 1771–1786 (2013).
40. Coogan, L. a. & Dosso, S. E. Alteration of ocean crust provides a strong temperature dependent feedback on the geological carbon cycle and is a primary driver of the Sr-isotopic composition of seawater. *Earth Planet. Sci. Lett.* **415,** 38–46 (2015).
41. Kelley, K. A., Plank, T., Ludden, J. & Staudigel, H. Composition of altered oceanic crust at ODP Sites 801 and 1149. *Geochem. Geophys. Geosyst.* **4,** 6 (2003).
42. Hammouda, T. High-pressure melting of carbonated eclogite and experimental constraints on carbon recycling and storage in the mantle. *Earth Planet. Sci. Lett.* **214,** 357–368 (2003).
43. Dasgupta, R., Hirschmann, M. M. & Withers, A. C. Deep global cycling of carbon constrained by the solidus of anhydrous carbonated eclogite under upper mantle conditions. *Earth Planet. Sci. Lett.* **227,** 73–85 (2004).
44. Yaxley, G. M. & Green, D. H. Experimental demonstration of refractory carbonate-bearing eclogite and siliceous melt in the subduction regime. *Earth Planet. Sci. Lett.* **128,** 313–325 (1994).
45. Dasgupta, R., Hirschmann, M. M. & Dellas, N. The effect of bulk composition on the solidus of carbonated eclogite from partial melting experiments at 3 GPa. *Contrib. Mineral. Petrol.* **149,** 288–305 (2005).
46. Gerbode, C. & Dasgupta, R. Carbonate-fluxed melting of MORB-like pyroxenite at 2.9 GPa and genesis of HIMU ocean island basalts. *J. Petrol.* **51,** 2067–2088 (2010).
47. Litasov, K. & Ohtani, E. The solidus of carbonated eclogite in the system $CaO–Al_2O_3–MgO–SiO_2–Na_2O–CO_2$ to 32 GPa and carbonatite liquid in the deep mantle. *Earth Planet. Sci. Lett.* **295,** 115–126 (2010).
48. Keshav, S. & Gudfinnsson, G. H. Experimentally dictated stability of carbonated oceanic crust to moderately great depths in the Earth: results from the solidus determination in the system $CaO–MgO–Al_2O_3–SiO_2–CO_2$. *J. Geophys. Res.* **115,** B05205 (2010).
49. Molina, J. F. & Poli, S. Carbonate stability and fluid composition in subducted oceanic crust: an experimental study on $H_2O–CO_2$ bearing basalts. *Earth Planet. Sci. Lett.* **176,** 295–310 (2000).
50. Connolly, J. A. D. Computation of phase equilibria by linear programming: a tool for geodynamic modeling and its application to subduction zone decarbonation. *Earth Planet. Sci. Lett.* **236,** 524–541 (2005).
51. Manning, C. E. Geochemistry: a piece of the deep carbon puzzle. *Nature Geosci.* **7,** 333–334 (2014).

52. Ague, J. J. & Nicolescu, S. Carbon dioxide released from subduction zones by fluid-mediated reactions. *Nature Geosci.* **7,** 355–360 (2014).
53. Manning, C. E. The chemistry of subduction-zone fluids. *Earth Planet. Sci. Lett.* **223,** 1–16 (2004).
54. Newton, R. C. & Manning, C. E. Quartz solubility in H_2O–NaCl and H_2O–CO_2 solutions at deep crust-upper mantle pressures and temperatures: 2–15 kbar and 500–900 °C. *Geochim. Cosmochim. Acta* **64,** 2993–3005 (2000).
55. Newton, R. C. & Manning, C. E. Solubility of enstatite + forsterite in H_2O at deep crust/upper mantle conditions: 4 to 15 kbar and 700 to 900 °C. *Geochim. Cosmochim. Acta* **66,** 4165–4176 (2002).
56. Newton, R. C. & Manning, C. E. Thermodynamics of SiO_2–H_2O fluid near the upper critical end point from quartz solubility measurements at 10 kbar. *Earth Planet. Sci. Lett.* **274,** 241–249 (2008).
57. Kessel, R., Schmidt, M., Ulmer, P. & Pettke, T. Trace element signature of subduction-zone fluids, melts and supercritical liquids at 120–180 km depth. *Nature* **437,** 724–727 (2005).
58. Stagno, V. *et al.* The oxygen fugacity at which graphite or diamond forms from carbonate-bearing melts in eclogitic rocks. *Contrib. Mineral. Petrol.* **169,** 16 (2015).
59. Zedgenizov, D. A., Kagi, H., Shatsky, V. S. & Ragozin, A. L. Local variations of carbon isotope composition in diamonds from São-Luis (Brazil): evidence for heterogenous carbon reservoir in sublithospheric mantle. *Chem. Geol.* **363,** 114–124 (2014).
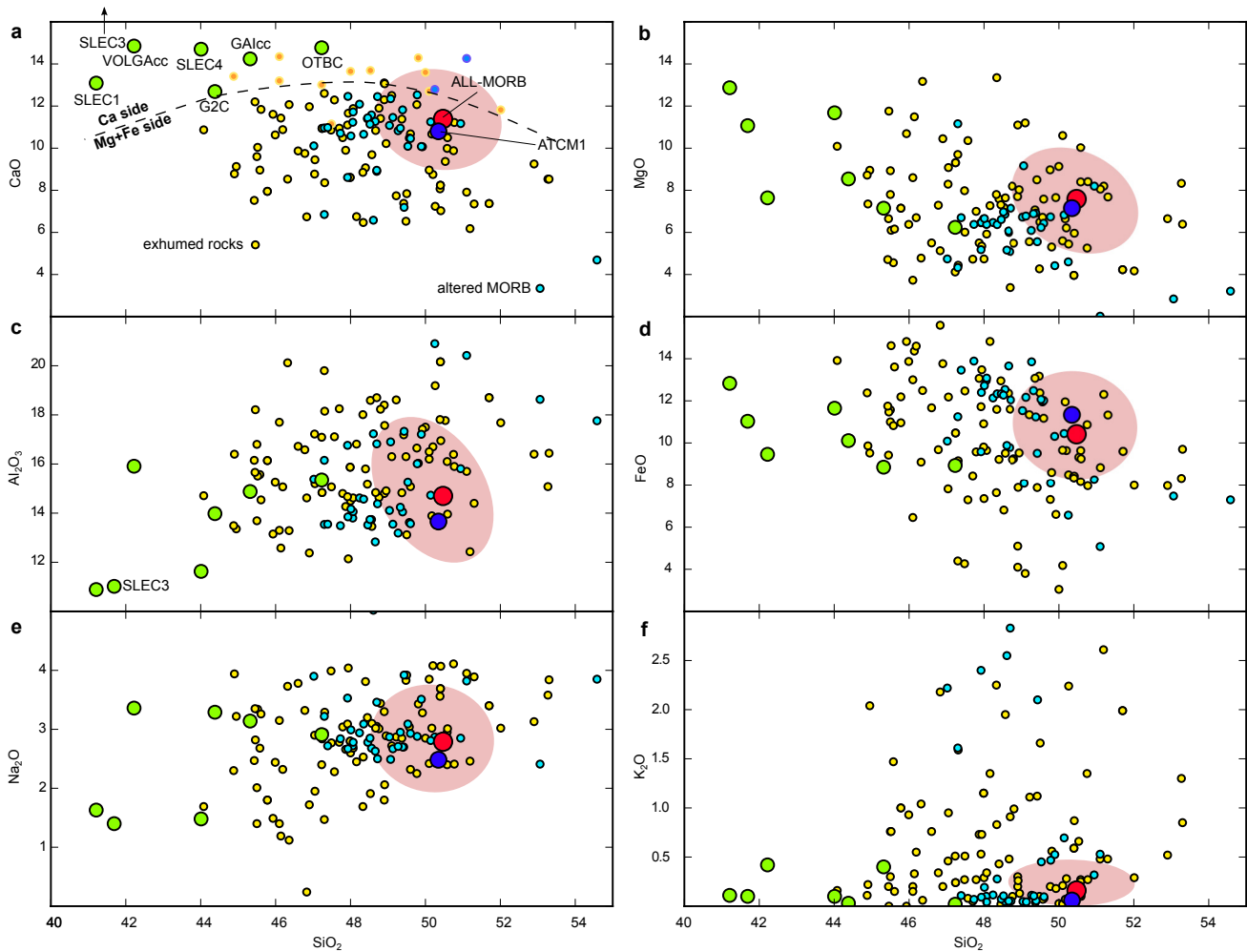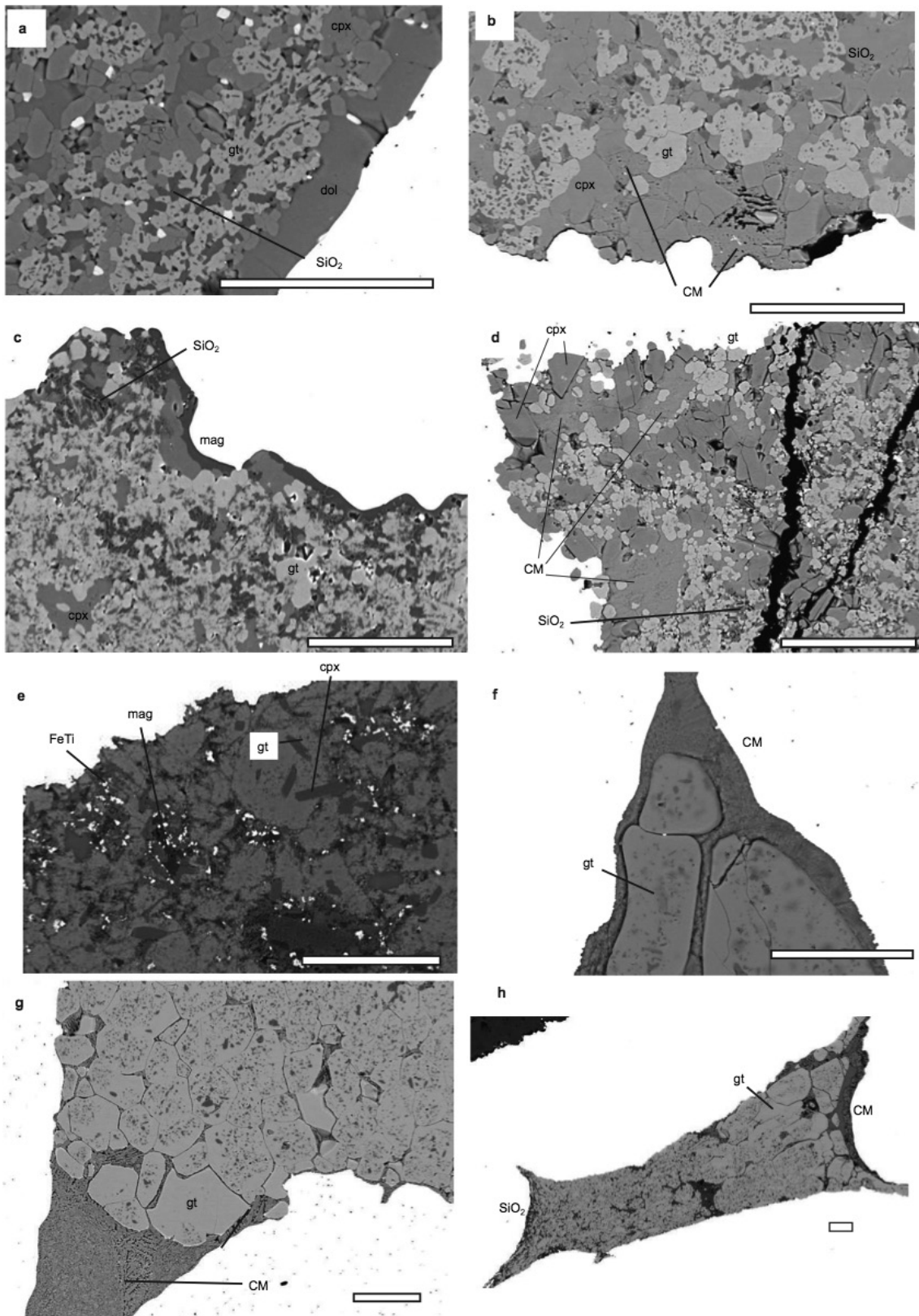
Extended Data Figure 1 | Comparison of experimental compositions with natural rocks. a–f, 'Fresh' MORB rocks (red field), ALL-MORB[21] (red circle), altered MORB rocks[41] (pale blue circles), exhumed blueschist, greenschist and/or eclogitic rocks (yellow circles) and starting material from this (dark blue circle) and previous studies (green circles) of carbonated MORB compositions. In **a**, rocks altered MORB and exhumed rock compositions that fall on the Mg-Fe side of the maj–cpx join from

Extended Data Fig. 5 plot below the dashed line, compositions that lie on the Ca side of this join are plotted as orange circles with yellow outlines or purple circles with blue outlines and sit above the dashed curve. This confirms that magnesite will be the stable carbonate phase at high pressure in the vast majority of natural crustal rocks, as is the case for ATCM1. Data and corresponding references for this figure are provided in the online source data file.
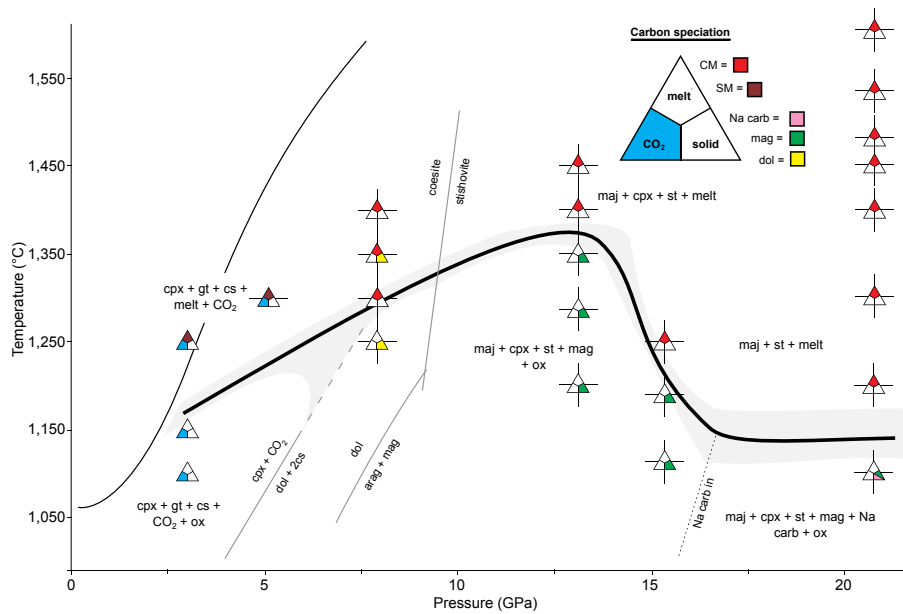
Extended Data Figure 2 | Experimental results/phase diagram and interpreted solidus position. The reactions clinopyroxene + CO_2 = dolomite + 2coesite and dolomite = magnesite + aragonite are from refs 22 and 23 respectively. The upper left curve is the anhydrous MORB solidus. Note that due to temperature gradients in experiments at 8 GPa, a small quantity of dolomite is observed coexisting with melt in one experiment above the solidus, present at the cold end of the capsule. arag, aragonite; CM, carbonatite melt; cpx, clinopyroxene; cs, coesite; dol, dolomite; gt, garnet; mag, magnesite; maj, majoritic garnet; Na carb, Na carbonate; ox, FeTi oxide; SM, silicate melt; st, stishovite.

Extended Data Figure 3 | BSE images of experimental products.
a, 7.9 GPa, 1,250 °C; **b**, 7.9 GPa, 1,350 °C; **c**, 13.1 GPa, 1,350 °C; **d**, 13.1 GPa; 1,450 °C; **e**, 20.7 GPa, 1,100 °C; **f**, 20.7 GPa, 1,480 °C; **g**, 20.7 GPa, 1,600 °C;

h, sandwich experiment, 20.7 GPa, 1,400 °C. Scale bars, 10 μm. CM, carbonatite melt; cpx, clinopyroxene; dol, dolomite; FeTi, FeTi oxide; gt, garnet; mag, magnesite.
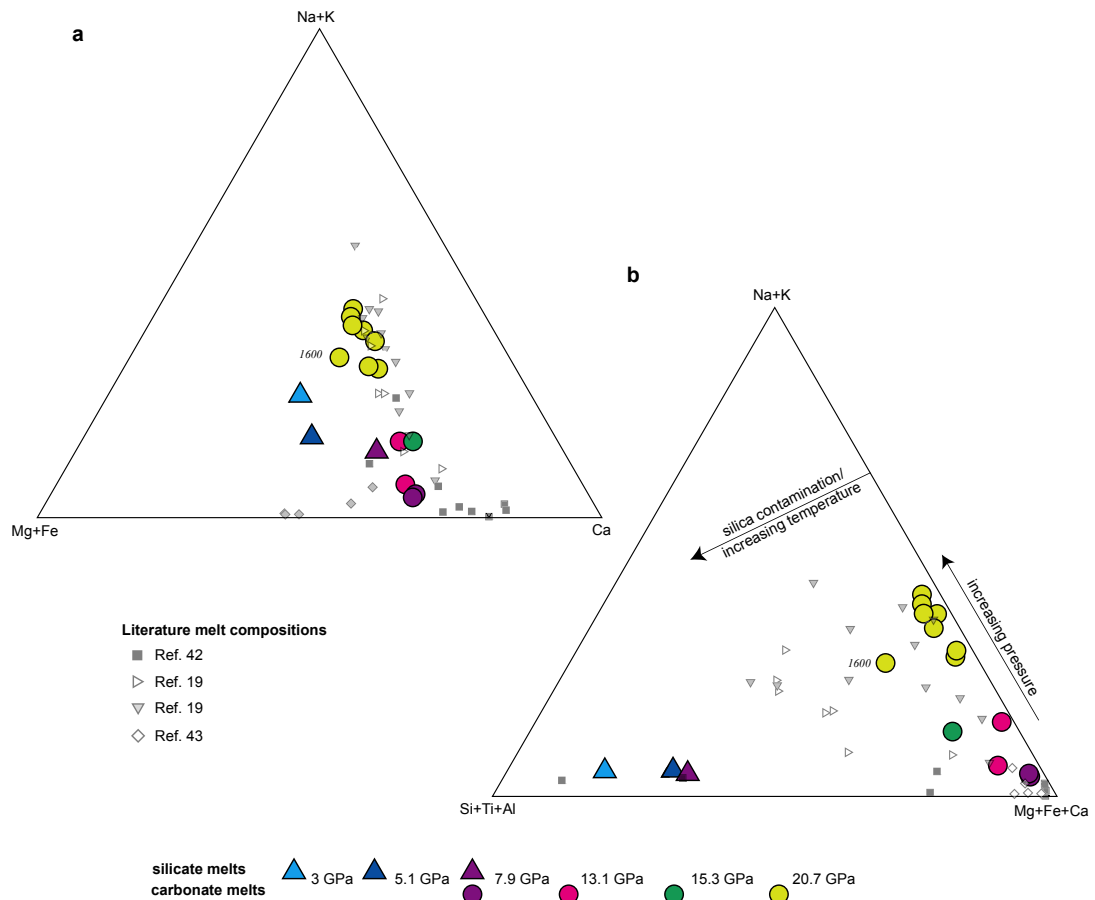
Extended Data Figure 4 | Composition of experimental melts from this study. a, b, Experimental melts from selected previous studies marked with semi-transparent greyscale symbols. **b,** The effects of increasing pressure, temperature and the effect of contamination due to partial analysis of silicate minerals surrounding small melt pools are shown.
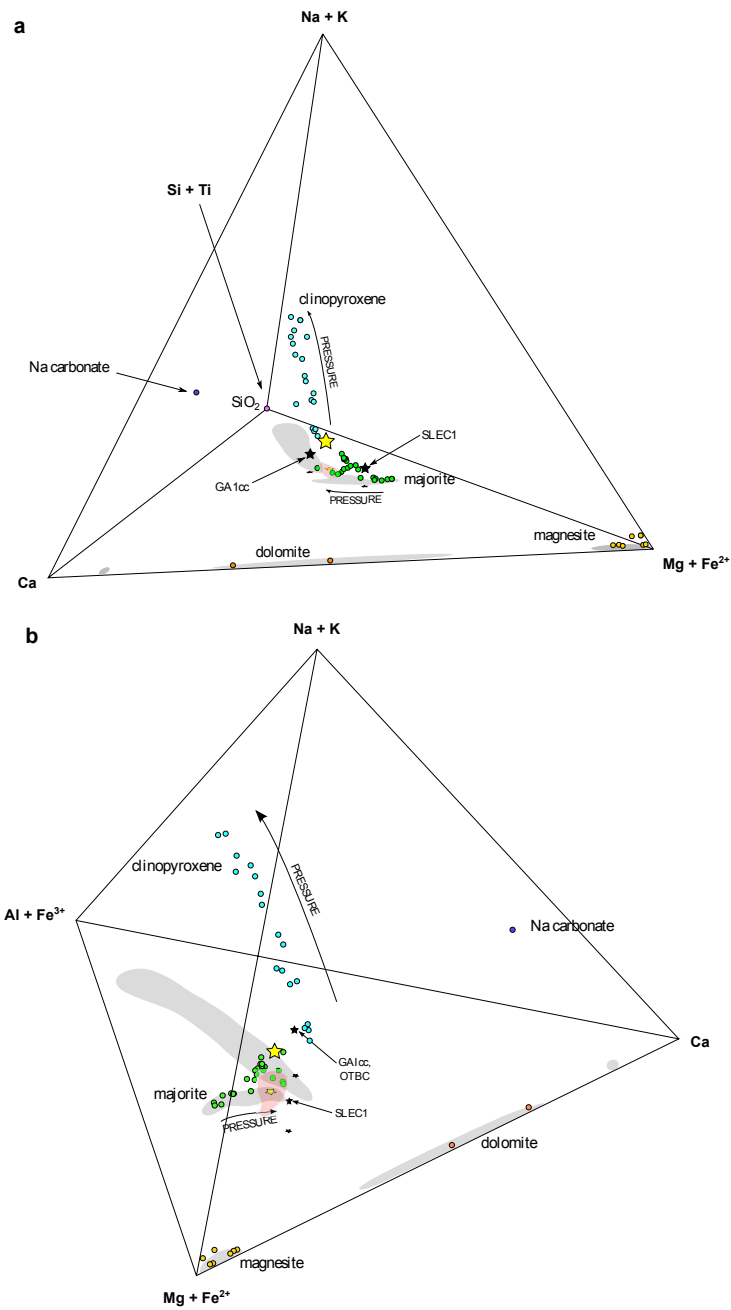
Extended Data Figure 5 | The composition of experimental phases from this study projected into two quaternary plots. a, b, [Ca]-[Mg+Fe^{2+}]-[Si+Ti]-[Na+K] (**a**) and [Mg+Fe^{2+}]-[Ca]-[Al+Fe^{3+}]-[Na+K] (**b**). In both diagrams the grey fields are the compositional data projected onto the basal ternary. The red field is the range of natural MORB compositions projected onto the basal ternary. The yellow star plotted in the four-component system and projected onto the basal ternary is ATCM1 (our bulk composition) while the black stars are bulk compositions from previous studies[25–27].
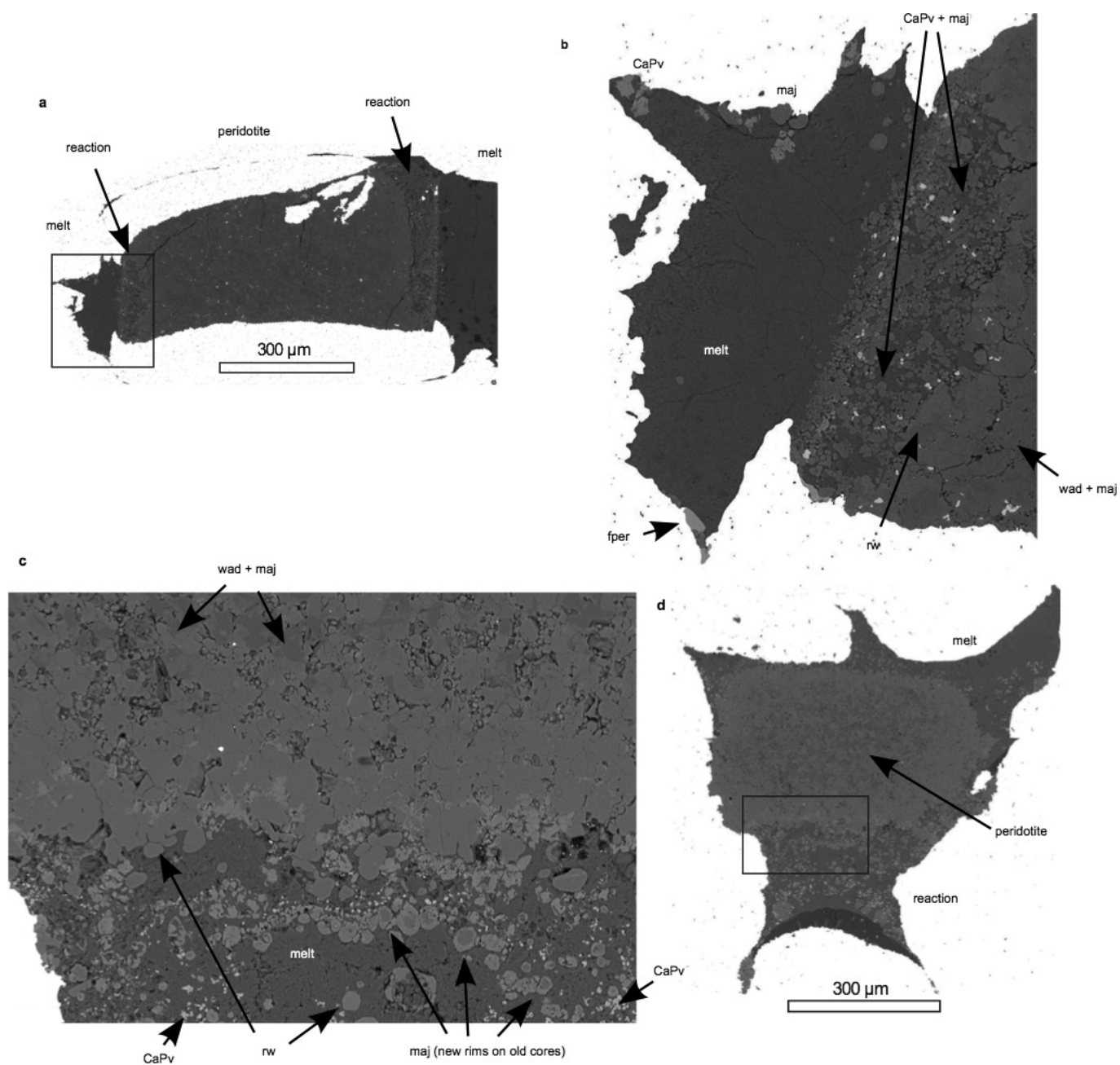
Extended Data Figure 6 | BSE images of reaction experiments.
a–d, G169 (a, b) and G177 (c, d). In both experiments a reaction zone and remaining carbonatite melt surrounds the unreacted peridotite region. a, An overview of G169. b, A close up of the reaction in G169 containing newly crystallized calcium perovskite, majorite, ferropericlase and ringwoodite minerals. c, A close up of the reaction products in G177, which consist of small bright calcium perovskites, new majorite that is often observed as a rim on relic peridotitic garnet and ringwoodite. d, An overview of G177. CaPv, calcium perovskite; fper, ferropericlase; maj, majorite; rw, ringwoodite; wad, wadsleyite.
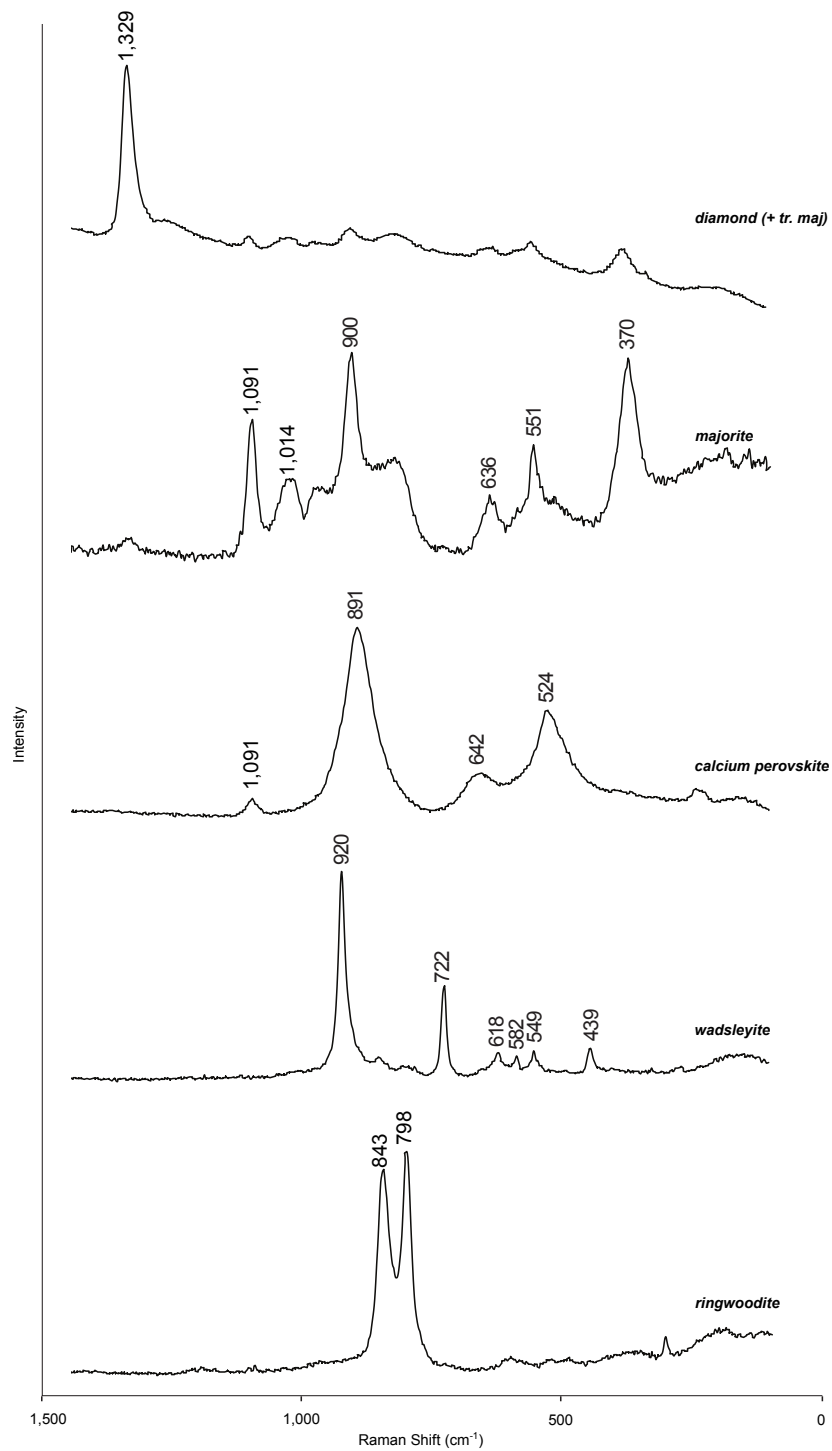
Extended Data Figure 7 | Raman spectra of minerals from reaction experiment G177 measured using a blue 455 cm^{-1} excitation laser. The position of the main peaks in each collected spectrum have been labelled with their shift from the excitation laser in cm^{-1}.
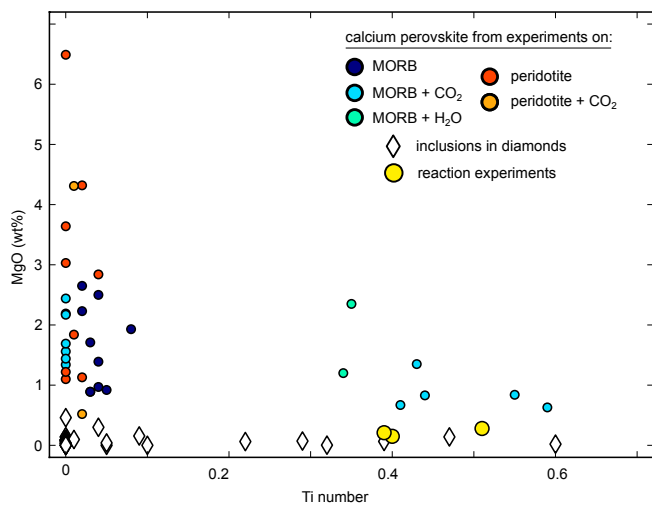
Extended Data Figure 8 | Comparison of diamond-hosted calcium perovskite inclusions with experimental mineral compositions in MgO versus Ti number space. Ti number = Ti/[Ca+Ti]. Data and corresponding references for this figure are provided in the online source data file.

Extended Data Table 1 | Starting materials used in this and previous studies

	ALL MORB[21]	IODP 1256 MORB[20]	ATCM1 (this study)	SLEC1[43]	OTBC[42]	GA1cc[19,41]	VOLGAcc[19]	SLEC2[45]	SLEC3[45]	SLEC4[45]	G2C[46]	ATCM2 (this study)	KR4003[31]	PM1[32]
SiO_2	50.47	51.48	50.35	41.21	47.23	45.32	42.22	30.29	41.69	44.01	44.38	0.71	44.90	45.74
TiO_2	1.68	1.44	1.33	2.16	-	1.34	1.43	1.58	2.18	2.31	1.75	1.52	0.16	0.21
Al_2O_3	14.70	14.18	13.66	10.89	15.35	14.88	15.91	7.95	11.02	11.63	13.98	0.33	4.26	5.01
Cr_2O_3													0.41	0.27
FeO	10.43	11.90	11.35	12.83	8.93	8.85	9.46	13.87	11.03	11.65	10.11	8.43	8.02	8.07
MnO	0.18	0.22	0.21	0.12	-	0.15	0.14	0.23	0.12	0.13	0.25	-	0.13	0.14
MgO	7.58	7.30	7.15	12.87	6.24	7.15	7.64	14.28	11.07	11.68	8.54	6.50	37.30	34.57
CaO	11.39	10.78	10.80	13.09	14.77	14.24	14.85	14.88	16.89	14.70	12.69	23.21	3.45	3.86
Na_2O	2.79	2.53	2.48	1.63	2.91	3.14	3.36	1.75	1.40	1.48	3.29	16.35	0.22	0.59
K_2O	0.16	0.06	0.06	0.11	0.02	0.40	0.42	0.13	0.10	0.10	0.03	0.57	0.09	0.08
P_2O_5	0.18	0.11	0.10			0.14	0.15					0.37		
NiO													0.24	0.20
CO_2			2.52	5.00	4.43	4.40	4.40	14.99	4.42	2.21	5.00	42.01		
Total	99.57	100.00	100.00	99.91	99.88	100.01	99.98	99.95	99.92	99.90	100.02	100.00	98.18	98.74
Ca#	0.38	0.36	0.36	0.32	0.48	0.46	0.45	0.33	0.41	0.37	0.39	0.60	0.06	0.07
Mg#	0.57	0.52	0.53	0.64	0.56	0.59	0.59	0.65	0.64	0.64	0.60	0.58	0.89	0.88

Ca number = Ca/[Ca+Mg+Fe]. Mg number = Mg/[Mg+Fe].

Extended Data Table 2 | Summary of run conditions and products for carbonated MORB melting experiments

	P (GPa)	T (°C)	time (min)	capsule	run products	comments	gt	cpx	cs/st	ox	dol	mag	Na carb	SM	CM	CO₂	r²
162G	3	1100	7200	Au₈₀Pd₂₀	gt, cpx, cs, rut, CO₂		29.96	59.02	7.84	0.24						2.52	0.12
161G	3	1150	7200	Au₈₀Pd₂₀	gt, cpx, cs, rut, CO₂		27.69	61.07	7.87	0.20						2.52	0.16
#5	3	1250	2880	Au₈₀Pd₂₀	gt, cpx, cs, rut, SM, CO₂		28.01	53.93	5.76	0.08				9.71		2.03	0.55
#32	5.1	1300	1560	Au₈₀Pd₂₀	gt, cpx, cs, rut, SM		30.22	40.81	7.92					20.97			0.20
#9	7.9	1250	1470	Au	maj, cpx, cs, rut, dol	dolomite segregated at one end	50.39	32.05	12.07	0.83	5.48						0.18
#10	7.9	1300	1440	Au	maj, cpx, cs, rut, CM	melt in centre (~25 °C above TC)	45.43	34.87	12.53	0.51					6.57		0.12
#14	7.9	1350	1770	Au₇₅Pd₂₅	maj, cpx, cs, rut, dol, CM	melt adjacent to TC, dolomite at cold end (~50 °C below TC)	44.49	34.96	13.62	0.63	1.95				4.42		0.11
#34	7.9	1400	1440	PtRe	maj, cpx, cs, CM	Fe loss to capsule											
#29	13.1	1200	1440	Au	maj, cpx, st, rut, mag	magnesite segregated at one end	64.37	14.85	15.31	0.49		4.75					0.39
#40	13.1	1280	120	Au	maj, cpx, st, rut, mag	Experiment failed after 2 hours	63.45	16.14	14.86	0.40		4.82					1.02
#12	13.1	1350	1440	Au	maj, cpx, st, rut, mag	magnesite segregated at one end	63.66	16.20	15.66	0.11		4.13					3.70
#39	13.1	1350	1560	Au	maj, cpx, st, rut, mag	repeat of #12	62.88	15.36	15.88	0.52		4.33					2.89
#17	13.1	1400	1440	Au	maj, cpx, st, CM	very small melt pools	61.89	18.82	15.27						6.45		0.34
#30	13.1	1450	1500	Au	maj, cpx, st, CM		63.69	15.55	14.60						5.86		0.10
#37	15.3	1115	2940	Au	maj, cpx, st, mag, FeTi oxide		65.50	14.56	14.00	0.87		4.52					0.77
#38	15.3	1190	3150	Au	maj, cpx, st, mag, FeTi oxide		64.39	12.04	17.38	0.39		5.44					0.23
#35	15.3	1250	1920	Au	maj, cpx, st, CM	small melt pools	64.14	13.50	15.74						6.31		0.13
#36	20.7	1100	3240	Au	maj, st, cpx, mag, Na carb, FeTi oxide		64.76	12.43	15.27	2.00		3.17	2.38				0.05
#27	20.7	1200	1440	Au	maj, st, CM	Re furnace, small melt pools	76.30		17.56						5.50		0.37
#28	20.7	1300	1440	Au	maj, st, CM	Re furnace	75.32		17.71						5.88		0.25
#19	20.7	1400	3660	Au	maj, st, CM		75.14		18.42						5.81		0.46
#11	20.7	1450	1440	Au	maj, st, CM		76.15		17.66						5.59		0.46
#13	20.7	1480	1650	Au	maj, st, CM		76.75		17.03						5.89		0.14
#16	20.7	1530	1440	Au	maj, st, CM	small melt pools	76.48		17.41						5.99		1.03
#31	20.7	1600	600	Au	maj, st, CM		75.10		17.28						7.37		0.34
#33	20.7	1400	1440	Au	maj, st, CM	75% ATCM1 + 25% ATCM2	61.48		10.41						27.58		2.16

Mass balance calculations were performed as described in Supplementary Information. Phase proportions are in wt%. CM, carbonatite melt; cpx, clinopyroxene; cs, coesite; dol, dolomite; FeTi oxide, iron-titanium-rich oxide phase; gt, garnet; mag, magnesite; maj, majoritic garnet; Na carb, sodic carbonate; rut, rutile; SM, silicate melt; st, stishovite.

Extended Data Table 3 | Summary of reaction experiments run conditions and experimental products

Type	Starting Material	Expt No.	T (°C)	Duration (mins)	Mineral phases
Synthesis	KR4003 + 2.5 wt.% Fe	G168	1600‡	510	wad, maj, capv, Fe
	``	G176	1590	480	wad, maj, CM*
Reaction	G168 + ATCM2	G169	1600	30	maj, capv, rw, fper, CM, maj†, wad†, capv†, Di*
	G176 + ATCM2	G177	1590	124	maj, capv, rw, mag, CM, Al$_2$O$_3$, maj†, wad†, Di*
Mixture	**PM1:ATCM2 (wt.%) in Fe capsules)**				
	9:1	Y17b	1400	180	fper, maj, rw, wad, capv*, melt, Fe, Di
	7:3	Y16a	1400	270	fper, maj, rw, wad, capv*, melt, Fe, Di
	1:1	Y16b	1400	270	fper, maj, rw, wad, capv*, melt, Fe, Di
	PM1:ATCM2:Fe (mol.%) in an Au capsule				
	16:4:1	G183b	1400		maj, rw, capv, mag, CM

capv, calcium perovskite; CM, carbonatite melt; Di, diamond; Fe, Fe metal; fper, ferropericlase; mag, magnesite; maj, majorite garnet; rw, ringwoodite; wad, wadsleyite.
*Trace/minor phase.
†Relics of the peridotite starting material.
‡Thermocouple broke during run; temperature estimated using power curves with maximum uncertainty of ±150 °C.